
Article:
Bastianini, F., Pérez, G.E. orcid.org/0000-0003-3150-8467, Hobson, A.R. et al. (5 more authors) (2019) In−situ monitoring Poly(3-hexylthiophene) nanowire formation and shape evolution in solution via small angle neutron scattering. Solar Energy Materials and Solar Cells, 202. ISSN 0927-0248

https://doi.org/10.1016/j.solmat.2019.110128

Graphical Abstract

In – situ monitoring Poly(3-hexylthiophene) nanowire formation and shape evolution in solution via Small Angle Neutron Scattering

Francesco Bastianini, Gabriel E. Pérez, Adam R. Hobson, Sarah E. Rogers, Andrew J. Parnell, Martin Grell, Alfredo Flores Gutiérrez, Alan D.F. Dunbar

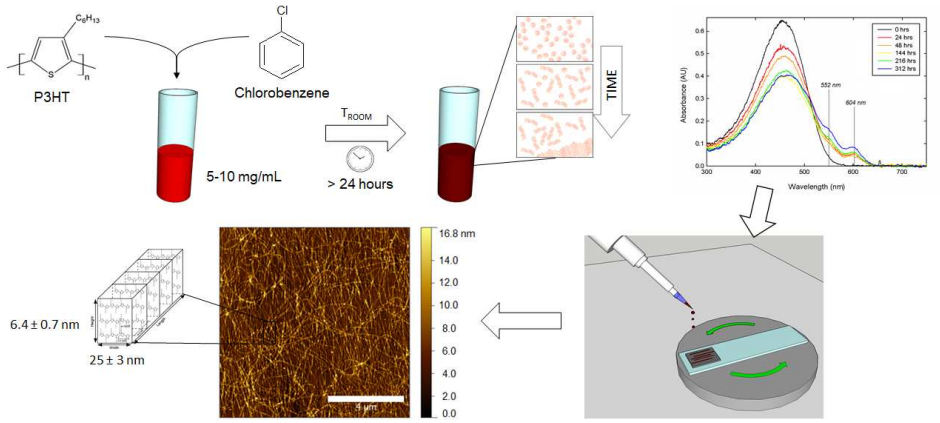

Highlights

$In-situ$ monitoring Poly(3-hexylthiophene) nanowire formation and shape evolution in solution via Small Angle Neutron Scattering

Francesco Bastianini, Gabriel E. Pérez, Adam R. Hobson, Sarah E. Rogers, Andrew J. Parnell, Martin Grell, Alfredo Flores Gutiérrez, Alan D.F. Dunbar

- Low temperature and time promote P3HT nanowires; high temperature dissolves them
- P3HT coils first elongate into nanorods, then assemble into lamellae and nanowires
- Model used allows spatial visualization of nanowire formation
- High spin coating speed results in improved nanowire alignment
- Deposition of selectively aligned P3HT nanowires improves thin film conductivity

$In - situ$ monitoring Poly(3-hexylthiophene) nanowire formation and shape evolution in solution via Small Angle Neutron Scattering

Francesco Bastianini[a], Gabriel E. Pérez[a], Adam R. Hobson[a], Sarah E. Rogers[b], Andrew J. Parnell[c], Martin Grell[c], Alfredo Flores Gutiérrez[c], Alan D.F. Dunbar[a]

[a]*Department of Chemical and Biological Engineering, The University of Sheffield, Mappin Street, Sheffield, S1 3JD, UK*
[b]*ISIS Neutron and Muon Source, STFC, Rutherford Appleton Laboratory, Didcot, OX11 0QX, UK*
[c]*Department of Physics and Astronomy, The University of Sheffield, Hounsfield Road, Sheffield, S3 7RH, UK*

Abstract

The crystallization of poly(3-hexylthiophene) (P3HT) to form nanowires has attracted considerable interest because this process significantly increases the hole mobility when compared to amorphous P3HT, leading to improved performance in photovoltaic and other organic electronic devices. However, full characterization of the crystallization self-assembly of the polymer chains in solution has not been achieved yet, due to limited use of $in - situ$ not destructive techniques. Here, we investigate the ageing-driven formation and evolution of regioregular (rr) P3HT nanostructures in chlorobenzene solution using small angle neutron scattering (SANS) and UV-Vis spectroscopy. We have monitored how the shape of the rr-P3HT aggregates evolve. The initial states for rr-P3HT chains are the random coils, which straighten to form rods. These subsequently π - π stack to form 2D lamellae, which further stack to create nanowires. The formation of nanowires is promoted both by the length of ageing and by low temperatures ($4°C$). Temperatures above $> 40°C$ reverse the formation of nanowires. Additionally, atomic force microscopy (AFM) and grazing incidence wide angle x-ray scattering (GIWAXS) reveal that the nanowires can be successfully aligned during deposition by off-axis spin coating. Finally, the anisotropic conductivity of the aligned rr-P3HT nanowire films is reported. This is significant for applications such as gas

sensing or organic thin film transistors, where increased conductivity and controlled nanostructure are desirable.

Keywords: P3HT, conjugated polymer, nanowires, small angle neutron scattering SANS, solution ageing, alignment

---

1. Introduction

The semiconducting polymer poly(3-hexylthiophene) (P3HT, figure 1a) has attracted considerable research interest because it is an effective electron donor and hole transporting material in photovoltaic devices Dang (2011); Onoda (1998); Berger (2018); Guo (2014); Xiao (2015); Zhou (2018); Poelking (2014); Laquai (2015); Agbolaghi (2017). Recently, P3HT as a material for solution processed solar cells has been superseded by other polymers such as Poly[N-9'-heptadecanyl-2,7-carbazole-alt-5,5-(4',7'-di-2-thienyl-2',1',3'-benzothiadiazole)] (PCDTBT) Wong (2017); Zhang (2016); Park (2009); Kwak (2016) and Poly[[4,8-bis[(2-ethylhexyl)oxy]benzo[1,2-b:4,5-b']dithiophene-2,6-diyl][3-fluoro-2-[(2-ethylhexyl)carbonyl] thieno[3,4-b]thiophenediyl]] (PTB7) Fernandes (2018); Liang (2010); Lu (2014), as well as organic - inorganic hybrid materials such as lead perovskite Wang (2015); Hu (2015); Wong (2018). However, P3HT has also shown promising potential in other applications such as organic field effect transistors Chu (2016), organic light emitting diodes Jeong (2011); Roige (2012); Kumar (2012), and vapor sensing devices Ellis (1996); Chan (2018); Im (2011). The presence of crystallinity within a P3HT thin film has a strong effect on its electronic properties and is known to improve device performance Seidler (2013); Bao (1996); Surin (2006). This improvement is due to increased hole mobility Joshi (2008); Woo (2012) caused by the formation of long crystalline nanowires which increase the interconnectivity of conductive pathways within the a device. The nanowires can increase the conductivity of the material as they provide an extended lower resistance channel for holes to be transported through a thin film compared to amorphous P3HT Poelking (2013). Therefore, understanding the formation of nanocrystalline P3HT structures and developing methods to improve the quantity and quality of nanowires in P3HT thin films remain a topic of considerable interest.

The formation of nanostructures commences as soon as the conditions of supersaturation in a suitable solvent are reached Newbloom (2014), and the polymer chains start to reorganize into more energetically favorable struc-

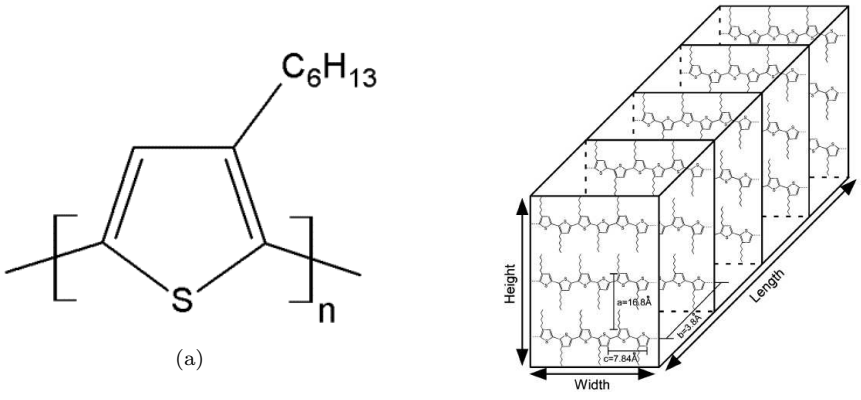

(a) (b)

Figure 1: ***Chemical structure of P3HT and representation of a P3HT nanowire.*** *(a) The repeating unit of the conjugated polymer P3HT and (b) a schematic diagram of the structure of a P3HT nanowire. Information from GIXD and TEM/XRD studies. Reprinted with permission from Merlo (2004). Copyright 2004 American Chemical Society.*

tures. Figure 1a shows the structure of P3HT, and figure 1b shows the structure of a P3HT nanowire Merlo (2004) (not dimensionally accurate). P3HT experiences lamellar stacking which gives the nanostructures greater height as shown in figure 1b. At the same time, the delocalized π electrons on neighboring molecular chains interact causing the P3HT chains to π - π stack to form long fibrous nanowires Merlo (2004); Dag (2010). Several solvents have been successfully employed for the formation of P3HT nanostructures, including toluene, xylene, chloroform, trichlorobenzene, dichlorobenzene, and chlorobenzene Kleinhenz (2015); Oh (2012); Newbloom (2014). In particular, chlorobenzene is a solvent widely used for P3HT, specifically for electronic applications.

Several processing conditions have been investigated in order to optimize this process and some have been shown to successfully promote nanowire formation such as the above mentioned favorable solvent selection Han (2015); Chang (2004), solution doping Kim (2010), use of ultrasound Xi (2018), use of an appropriate film deposition technique Diao (2014); Katz (2004), and post-treatments such as thermal Cho (2006); Cui (2003) and solvent annealing Fu (2015); Dickey (2006); Hu (2014). A long-term ($>$ 2 hours) ageing of the P3HT solution to self-assemble nanowires is one of the simplest methods of P3HT nanowire formation. This method promotes nanowire growth without the need for additional treatments or dopants, and it is not limited

to the deposition technique, simplifying in this way the device fabrication process considerably.

Despite the interest in P3HT nanowires, a small amount of work has been reported on monitoring the self assembly process directly in solution. $Ex-situ$ analysis allows observation of the nanowires only after they passed through several processes (*e.g.* deposition and drying), that could have significantly altered the structure Newbloom (2011). In contrast, $in-situ$ techniques directly monitor the nanowires in solution. SANS (small angle neutron scattering) distinguishes itself amongst the $in-situ$ techniques for the passive interaction with the system under study, the possibility to simultaneously investigate a wide range of length scales, and the significant penetration of neutrons into chlorine-based solvents, which makes SANS more suitable than small angle X-ray scattering Newbloom (2012); Keum (2013); Bernardo (2018). Previous studies have reported measurements and modelling of P3HT nanowire self-assembly via SANS, under different conditions: P3HT concentration, solvent Newbloom (2011), or different compositions of a mixture of solvents Keum (2013); Newbloom (2014). However, other parameters fundamental for the growth of P3HT nanowires have not been as widely studied. Temperature has been studied over a limited range Newbloom (2012), and the ageing time has been reported only once Newbloom (2014).

In addition to the ability of P3HT to self-assemble into nanowires in solution, the possibility of transferring these nanowires onto substrates with the nanowires aligned along a preferential direction plays an important role influencing the charge transport properties within the final applications Dorling (2014); Lee (2011); Giri (2015); Na (2015). Charge transport is dependent on crystal morphology, grain boundary effects, and inter-crystal morphology Jimison (2009); Chang (2013). Several techniques have been successfully employed to create aligned P3HT thin films, for example blade coating Chu (2016), deposition under electric fields Xi (2017), spin coating Yuan (2014); Kim (2015), mechanical stretching Chu (2016), and use of rubbed templates Dorling (2014). In particular, spin coating appears to be the most desirable, due to its simplicity, accurate reproducibility, and highly controllable parameters such as thickness. Conventional on-center spin coating produces a network of randomly aligned nanowires. In order to align the nanowires on the substrate, an off-center technique was developed Yuan (2014); Kim (2015), whilst keeping the experimental apparatus simple and guaranteeing optimal properties of the deposited material, specifically its electrical prop-

erties.

In this work, we have studied the growth of regioregular (rr) P3HT (96.6% regioregularity, $M_{\mathrm{w}} = 65,500$, $M_{\mathrm{n}} = 32,000$) nanowires in chlorobenzene during long-term solution ageing using UV-Vis spectroscopy and small angle neutron scattering (SANS). Conditions under which extensive nanowire networks form in solution without the need for any treatment are identified. Additionally, with SANS we are able to follow directly the evolution of the geometrical shape of the rr-P3HT, as a function of the thermal history, varying simultaneously the ageing time and the temperature. Furthermore, we have deposited aligned rr-P3HT nanowires from nanowire-rich solution via two techniques: on-center spin coating, where a spin speed threshold for radial alignment has been found, and off-center spin coating. The preferential alignment and the anisotropic properties are confirmed by atomic force microscopy (AFM), grazing incidence wide angle X-ray scattering (GIWAXS), and electrical conductivity measurements. The increase in conductivity and the control of structure formation during crystallization may be beneficial for electronic applications of rr-P3HT.

2. Results and discussion

2.1. UV-Vis spectroscopy

In order to verify that ageing promotes nanowire growth of rr-P3HT in chlorobenzene and to determine the time scale of this phenomenon, we measured the UV-Vis absorption spectra of a $10mg/mL$ solution at six time points during a 312 hours period. Each measurement was done by extracting a small sample from the $10mg/mL$ solution at each time step and diluting it to $0.02mg/mL$, to allow significant light to transit through the strongly absorbing solution to permit meaningful absorbance spectra to be recorded. As can be observed in figure 2, the 0 hours (as prepared) sample exhibits a single broad absorption peak which is an indication of good dissolution of the rr-P3HT in the solvent Fei (2015), suggesting that there is no aggregation or crystallinity present in the sample. However after 24 hours the absorption spectrum of the solution reveals one shoulder at $552nm$ and a small peak at $604nm$ which are attributed to P3HT $\pi - \pi^*$ transitions Shrotriya (2005); Zhao (2010). The appearance of these vibronic peaks indicates that there is aggregation in the solution and a higher degree of ordering of the polymer chains Kim (2015), which is a sign of increased crystallinity and nanowire formation. As the solution continues to age, the intensities of the second and

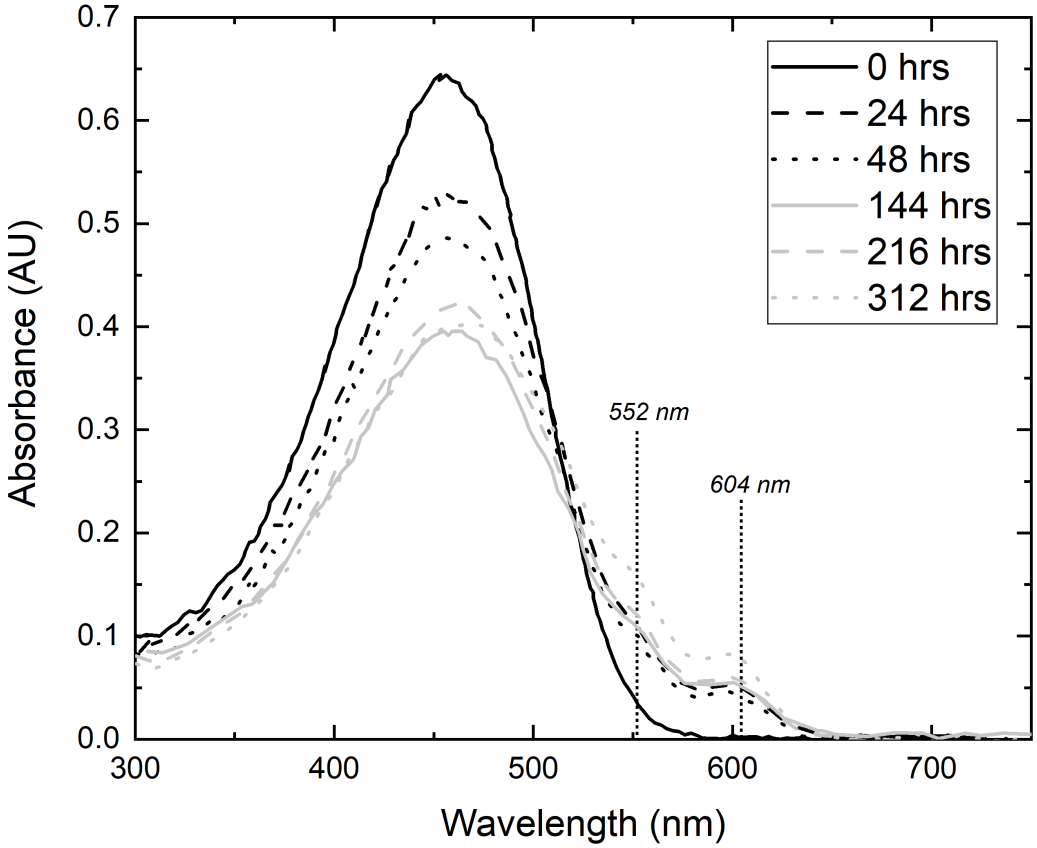

Figure 2: ***UV-Vis absorbance.*** *UV-Vis spectroscopy absorption data showing the evolution of the absorbance spectrum of* $10mg/ml$ *rr-P3HT in chlorobenzene over a period of* 13 *days.*

third peaks increase as shown after 48 hrs, 144 hrs, and 216 hrs, evidencing further nanowire growth and improved rr-P3HT crystallinity. However, the increase in intensity of the peaks from those samples is smaller, implying that the formation of $\pi - \pi^*$ stacked lamellae is fast during the first 24 hours, and decreases with time thereafter. Nonetheless, the 312 hours data confirm that nanowire formation will continue as the solution ages, since its absorption spectrum exhibits further higher intensities for the second and third peaks.

2.2. Small Angle Neutron Scattering

In order to understand nanowire formation by solution ageing, we studied their growth at the molecular length scale using small angle neutron scat-

tering (SANS). This was done by fitting the obtained 1D scattering plots with the Guinier-Porod function Hammouda (2010); Hammoudabis (2010) which can be used as an empirical model to determine the dimensionality of the scattering objects. This function is a combination of the Guinier and Porod models. The Guinier model is a standard model used to determine the dimension of dilute, monodisperse spheres of coiled polymers Guiner (1955), while the Porod model is used for elongated objects such as uncoiled polymer chains, lamellar structures, and nanowires Feigin (1987). The combined function includes a Porod exponent to determine the degree of elongation of the polymer chains and lamellar stacking to form nanowires in a lamellar Porod regime Hammouda (2010). The Guinier-Porod model makes it possible to follow the nanowire growth process from the Guinier regime when the rr-P3HT molecules exist as small and almost point like objects (discrete polymer coils), through the Porod regime as the P3HT elongates into rods which $\pi - \pi^*$ stack to form lamellae and eventually forming nanowires, which are readily observed upon spin coating (see figure 7a). Based on the generalized Guinier law for such elongated objects Guiner (1955); Glatter (1982), one can obtain the Porod-Guinier equations:

$$I(Q) = \begin{cases} \frac{G}{Q^s} \exp\left(\frac{-Q^2 R_g^2}{3-s}\right), Q \leq Q_1 \\ \frac{D}{Q^m}, Q \geq Q_1 \end{cases} \tag{1}$$

where two boundary conditions must be satisfied:

$$Q_1 = \frac{1}{R_g}\left[\frac{(m-s)(3-s)}{2}\right]^{1/2} \tag{2}$$

and:

$$D = \frac{G}{{R_g}^{(m-s)}} \exp\left[-\frac{m-s}{2}\right]\left[\frac{(m-s)(3-s)}{2}\right]^{\frac{m-s}{2}} \tag{3}$$

Where $I(Q)$ is the scattered intensity, Q is the scattering variable, R_g is the radius of gyration, m is the Porod exponent, G and D are the Guinier and Porod scale factors, respectively, and s is a dimensionality factor Hammouda (2010). Our main focus was on the s factor since it gives information on the shape of the observed objects. All the parameters obtained from the modelling can be found in table S1 in the supporting information document. For any given scattering sample, an s value of 0 indicates globular objects

extended in 0 macroscopic dimensions such as spherical polymer coils in the solution; an s value of 1 indicates objects elongated in 1D, such as rods; and finally an s value of 2 suggests 2D objects, for example lamellae or platelets. Values of s between these integer values indicate that there is a mixture of dimensional symmetries present. Additionally, the Porod exponent m contains information about the origin of the scattering features Hammouda (2010). For example, $m = 4$ indicates point like particles, $m = 2$ Gaussian polymer coils or 2D objects (lamellae) at low Q, and $m = 1$ stiff rods.

Firstly, the growth of nanowires in a solution aged over a time period of 17.7 hours was monitored by measuring a fresh (as prepared) $3mg/mL$ rr-P3HT solution three times overall this period. In order to achieve sufficient contrast between rr-P3HT and the solvent the solution was prepared by dissolving rr-P3HT into deuterated (d_5) chlorobenzene. In this first experiment, a lower concentration was used, as this was proved to hinder the nanowire formation process Malik (2004). A possible slowing down of nanowire formation was considered beneficial due to the long measurement times needed for neutron experiment. However, the formation was sufficiently slow to follow with SANS analysis, so for all subsequent SANS the standard $5mg/mL$ was used. The rr-P3HT was dissolved at $80°C$, filtered, and cooled down to $25°C$. This temperature was maintained constant during the subsequent measurements. For each measurement, data were collected for 1.87, 1.07, and 1.02 hours after 0, 9.32, and 16.68 hours respectively (figure 3). According to the Guinier Porod model fit, the dimensionality factor of the freshly prepared sample (0 hours) was 0.58 ± 0.14. This suggests that the distribution of objects within the solution is partway between 0D and 1D structures. These objects can be interpreted as spheres and rods indicating that the polymer chains start to uncoil and elongate into rods as soon as the solution is cooled to $25°C$. After 9.32 hours, the solution data showed an increased s factor of 0.88 ± 0.08 demonstrating that increased rod formation has occurred during the ageing period. This was further confirmed by the data collected after 16.68 hours which had an s factor of 1.00 ± 0.02, corresponding to a regime comprised of virtually only rods, demonstrating that after a further 6.3 hours of ageing, the morphology had become that of entirely rod-like structures. These results are summarized in table 1, and prove the extensive formation of rods within first hours of ageing.

To corroborate the findings from UV-Vis, a second solution for SANS with increased concentration was measured after one week of ageing. A solution of $5mg/mL$ of rr-P3HT in deuterated (d_5) chlorobenzene was stored for 7 days

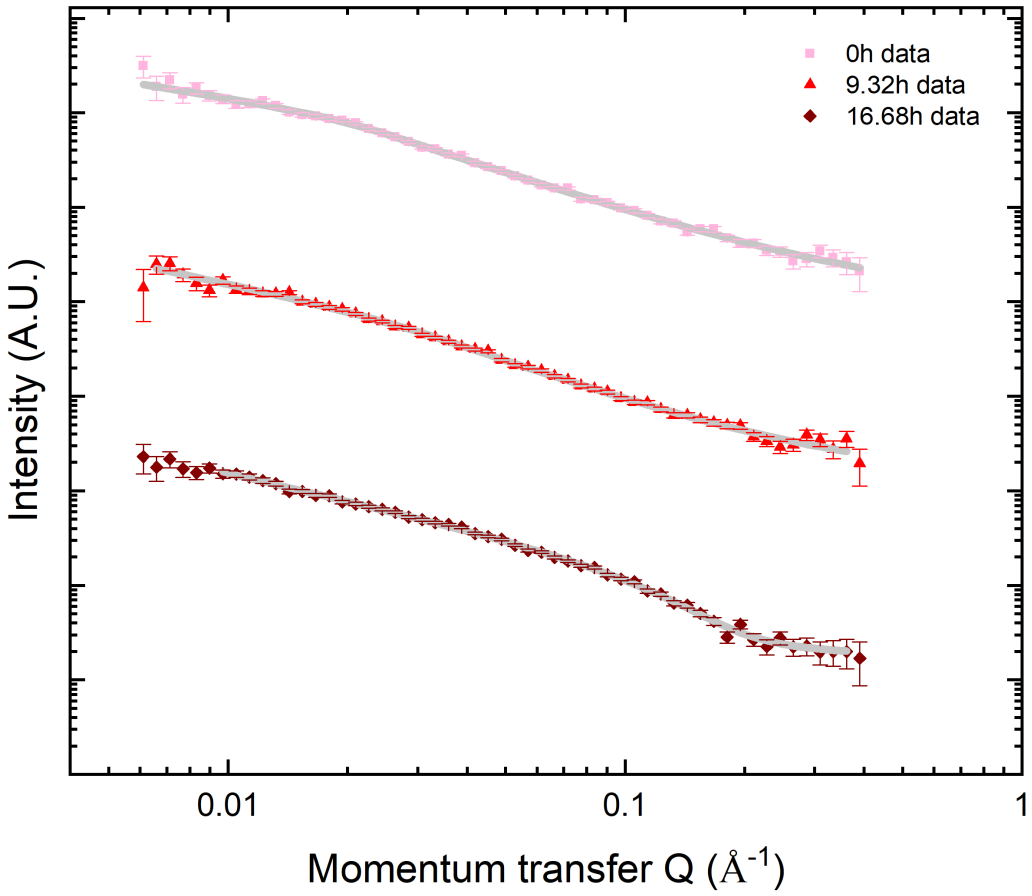

Figure 3: ***SANS of fresh P3HT solution.*** *SANS data and their corresponding fits (gray) of the freshly prepared rr-P3HT solution collected three times after 0 hours (pink), 9.32 hours (red), and 16.68 hours (claret), during a* 17.7 *hours period while kept at* $25°C$*. The three measurements are shown offset by two decades from each other to enable comparison.*

Table 1: *Dimensionality factors (s) resulting from applying the Guinier Porod function to fit the three SANS data sets collected for the fresh rr-P3HT solution over a period of* 17.7 *hours. Temperature and interpretation of the contents of the solution are also shown for comparison.*

Time (hrs.)	Temperature (°C)	s factor	Morphology
0	25	0.58 ± 0.14	slight majority of rods, and spheres
9.32	25	0.88 ± 0.08	mostly rods
16.68	25	1.00 ± 0.02	rods

Table 2: *Dimensionality factors (s) resulting from applying the Guinier Porod function to fit the three SANS data sets collected for the one week aged rr-P3HT solution at temperatures of* $18°C$, $25°C$ *or* $-2°C$ *over a period of* 181.93 *hours.*

Time (hrs.)	Temperature (°C)	s factor	Morphology
168	18 (ageing), 25 (measure)	1.29 ± 0.11	mostly rods, and lamellae
169.5	25	1.10 ± 0.13	mostly rods, and lamellae
181.57	25 after -2	1.39 ± 0.19	majority of rods, and lamellae

at $18°C$. This concentration has been chosen because it is within the typical range for P3HT in solution Chu (2016); Kim (2015); Heo (2018); Newbloom (2011). The solution was then loaded into the sample chamber and kept at a constant temperature of $25°C$ during 0.37 period of data collection. Figure 4 shows the scattering plot for the sample along with its corresponding fit. According to the Guinier Porod model fit, the dimensionality factor was 1.29 ± 0.11 which suggests a system comprised mostly of 1D objects, but 2D objects as well (table 2). Compared to the freshly prepared sample shown in table 1 the s factor of the one week aged solution is higher. While s factor increases from 0 to 1 indicate the evolution of polymer chains from spherical random coils towards elongated rods, further increases towards 2 represent the π - π stacking of rods into lamellar structures. The lamellae can ultimately stack into a nanowire. This confirms our findings from the UV-Vis section that a suitably long ageing period promotes nanowire formation. A second measurement (lasting 0.52 hours) was performed after that the solution was kept at $25°C$ for 1.13 hours. The dimensionality factor was 1.10 ± 0.13, slightly lower than the previous one, but still in the mixed regime of rod-like and lamellar structures. Therefore, the s factor has changed after a period at higher temperature, an indication that the dimensionality of the nanostructures depends on the temperature. In order to validate this, a third measurement was taken also at $25°C$, but after a short period (0.55 hours) at significantly lower temperature ($-2°C$). The temperature was then set back to $25°C$ for the 0.37 hour measurement. The dimensionality factor of 1.39 ± 0.19 suggests that more rr-P3HT chains had assembled into lamellar structures due to the cooling process, evidencing that decreases in temperature significantly promote lamella formation and therefore nanowire growth.

The effect of solution temperature on nanowire formation was more systematically investigated by preparing a fresh $5mg/mL$ solution, and mea-

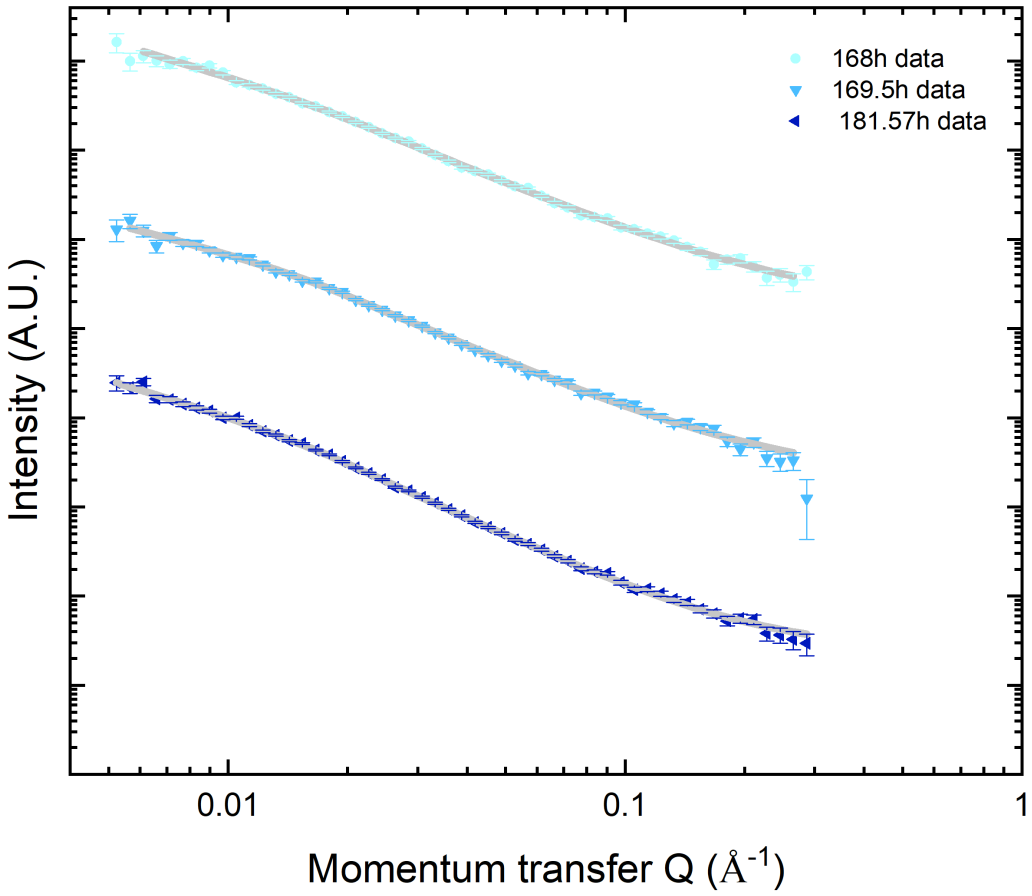

Figure 4: ***SANS of 1 week aged P3HT solution.*** *SANS data and their corresponding fits (gray) of the one week aged rr-P3HT solution collected three times after a total ageing of 168 hours (light blue), 169.5 hours (azure), and 181.57 hours (dark blue). The solution was kept at* $18°C$ *during the ageing, at* $25°C$ *during the measurements, and dropped for* $33min$ *at* $-2°C$ *just before the third measurement. The three measurements are shown offset by two decades from each other to enable comparison.*

suring it 8 times during a period of 42.77 hours at different temperatures (see figure 5 and table 3). During the first step, the solution was kept at $75°C$ for 7.5 hours, and measured twice for 0.75 hours, after 3.45 and 6.75 hours. In the supporting information, Figure S1 shows the data collected for the two measurements, and the corresponding fits for all the SANS measurements are reported in table T1. The dimensionality factors of the data collected were 0.48 ± 0.12 and 0.38 ± 0.16, for the 3.45 hours and the 6.75 hours measurements, respectively. These values indicate a regime between that of globular or spherical scattering objects, and that of rods. As we expected, this suggests that the formation of nanowires has not been able to proceed due to the high temperature, that keeps the polymer solubility high, and prevents aggregation of the rr-P3HT chains. The decrease in s factor for the second measurements could indicate further dissolution of polymer towards spherical structures, but a more final conclusion is prevented by the values being within error estimations.

For the second temperature step, the sample chamber was cooled down to $4°C$ during a 1 hour ramp, and kept at that temperature for an additional time of 29.93 hours. During this time, data were collected for 1 hour three times at total times of 9.5, 17.5, and 36.5 hours respectively (see supporting information, figure S2). The s factors of the sample at the three different times were 0.52 ± 0.14, 1.39 ± 0.03, and 1.52 ± 0.04, respectively. The small increase of the s factor from the final high temperature measurement at 6.75 hours, to the first low temperature measurement at 9.5 hours indicates a slight reduction in the presence of spherical objects (polymer coils) in solution and the appearance of some rod-like structures, suggesting that the decrease in temperature has already started to promote chain elongation, although it is noted this change is relatively small. The positive effect that lowering the temperature has on nanowire formation is demonstrated by the further increase in the s factor when the sample is maintained at $4°C$ for the 17.5 hour and 36.5 hour measurements. There is a significant increase in s indicating the presence of lamellar structures and nanowires already at 17.5 hours (9 hours at $4°C$). This is a clear indication that a prolonged period of time at low temperature is highly beneficial for nanowire formation.

During the last step, the sample chamber temperature was stepwise increased to $20°C$, $40°C$, $60°C$ and $80°C$, with ramps of 0.17 hours. The temperature was held at each of these increments for 0.92 hours for data collection. Three measurements were taken at 38.6, 39.68, and 41.85 hours, corresponding to $20°C$, $40°C$, and $80°C$ (see figure S3 in supporting informa-

Table 3: *Dimensionality factors (s) resulting from applying the Guinier Porod function to fit the SANS data sets collected for the fresh rr-P3HT solution. Temperature and time for each result are shown for comparison*

Time (hrs.)	Temperature (°C)	s factor	Morphology
3.45	75	0.48 ± 0.12	spheres and rods
6.75	75	0.38 ± 0.16	majority of spheres, and rods
9.5	4	0.52 ± 0.14	spheres and rods
17.5	4	0.93 ± 0.40	rods
36.5	4	1.52 ± 0.05	rods and lamellae
38.6	20	1.39 ± 0.05	majority of rods, and lamellae
39.68	40	0.49 ± 0.13	spheres and rods
41.85	80	0.28 ± 0.16	majority of spheres, and rods

tion). The corresponding dimensionality factors were 1.39 ± 0.05, 0.49 ± 0.13, and 0.28 ± 0.16, respectively. The slight decrease of the s factor between the previous $4°C$, measurement and the $20°C$ measurement suggests a small decrease of lamellar structures in the solution attributed to nanowires re-dissolving due to increasing temperature. The removal of nanowire structures by increasing the temperature is evident with the dramatic drop in s factor between $20°C$ and $80°C$, suggesting a rapid disappearance of lamellar structures. At $40°C$ there is an evenly mixed regime of rod-like and spherical objects. At $80°C$ the P3HT has mainly re-dissolved, therefore the majority of the rr-P3HT is present in the shape of sphere-like objects. All these results highlight the important role of temperature plays in the formation and the shape of rr-P3HT nanostructures in solution, and that a strong asymmetry exists between formation and dissolution of nanostructures. Formation of rr-P3HT nanostructures during cooling is much slower than dissolution during heating.

The results from the analysis of s values are supported by the interpretation of the Porod exponent m. As one can see in table S1 in the supporting information and in figure 5, m usually follows the same trends as s, increasing when s increases. Values of $s = 2$ indicate the presence of lamellae. At high temperature $40 - 80°C$ these disappear and m is closer to 1 which indicates rods. Note that at 16.68 hours in table 1, m is equal to 4, but in this case the fit is poor, and the errors for m are very large.

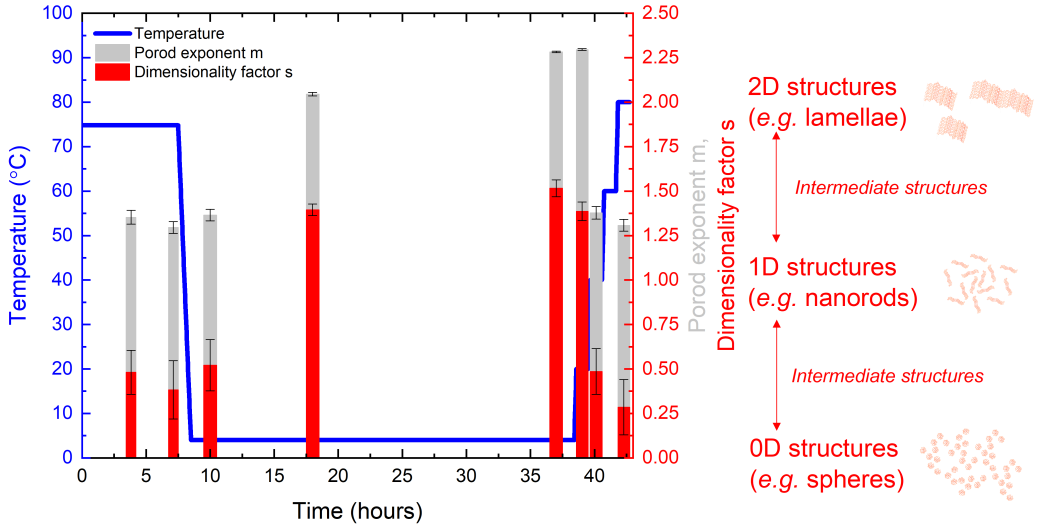

Figure 5: ***Evolution of s factor with time and temperature.*** *Temperature (blue line and scale), m exponent (gray bars and red scale) and dimensionality factor s (red bars and scale) as a function of the ageing time of a* $5mg/mL$ *rr-P3HT solution.*

2.3. Alignment of nanowires in thin films

Nanowires formed in a solution aged for long period of time were deposited as thin films and their alignment as a function of spin speed was investigated by atomic force microscopy (AFM). A one month aged $5mg/mL$ rr-P3HT solution in chlorobenzene was on-center spin-coated at 1000, 2000, 4000, and $5000rpm$. As shown in figures 6a and 6b, at low spin speeds (1000 and $2000rpm$) some of the nanowires are aligned, mainly those close to the substrate, but most of the nanowires have a random direction throughout the film. The nanowires closest to the substrate are most likely to align along the radial flow direction suggesting that the alignment is a result of pinning to the substrate and then being drawn out in the radial direction by the flowing solution. When the film is spin-coated at higher speeds ($> 4000rpm$) a clearer pattern of preferential alignment for the nanowires appears on the film, especially towards the edge of the substrates, as shown in figures 6c and 6d. The dependence of nanowire alignment on spin speed can be attributed to the magnitude of the centripetal and centrifugal forces. At lower speeds these forces seem insufficient to align the nanowires in the radial direction. However, as the spin speed increases, the magnitude of the radial forces increases, becoming capable of forcing the nanowires to align in the radial

direction.

The typical height and width of nanowires were determined by analyzing the height profiles across selected nanowires. In order to obtain high quality nanowires but with low density so that we can isolate them for analysis, we stored a $10mg/mL$ at $4°C$ for 27 days, and then diluted it to $1.67mg/mL$ for spin-coating at $5000rpm$ for $60sec$. Initially, 8 homogeneous sections of nanowire in a single image 7a were selected, and their profiles obtained by averaging the height profile along a constant length of the respective nanowires (the length of the sections averaged is indicated by the bars in figure 7a). Subsequently, the nanowires with profiles 1 to 5 were identified as being exposed on the surface, whereas profiles 6 to 8 belonging to nanowires partially embedded within an amorphous layer of rr-P3HT, and therefore not an accurate representation of the nanowire population. Lastly, the overall average height and average width were calculated: the average height by averaging the maximum values of profiles 1 to 5, and the average width by averaging the full width at half maximum height values of the same profiles (figure 7b). The overall average height and width of nanowires were found to be 6.4 ± 0.7 and $25 \pm 3nm$, respectively. These height and width values for nanowires agree with those reported in literature given that the width of the nanowire is proportional to the average molecular weight of the polymer, *i.e.* dependent upon the average polymer chain length Oosterbaan (2009).

2.4. Conductivity dependence of nanowires on directional alignment

In order to confirm possible electrical anisotropy arising from nanowire alignment, nanowires were deposited on ten different glass substrates each with two lithographically defined rectangular gold electrodes separated by a $10\mu m$ gap. The substrates were positioned $2cm$ away from the center of rotation of the spin coater Yuan (2014); Kim (2015), with the gap between electrodes aligned in two possible ways: either parallel to the radial direction (substrate on the right in figure 8) or perpendicular (substrate on the left). In total, 5 samples were deposited for each configuration, from a $5mg/mL$ 1 month aged solution cast at $5000rpm$, which generates a centripetal acceleration of $139m/s^2$. AFM height images of the nanowire coated samples, shown in figure 9, confirm that the nanowires align along the radial direction of rotation. Therefore the nanowires are oriented perpendicular across (figure 9a) or parallel along (figure 9b) the gap between the electrodes.

Once prepared, each of the 10 samples was subjected to a $-1V$ to $1V$ voltage sweep across the gap between the electrodes. The averaged current-

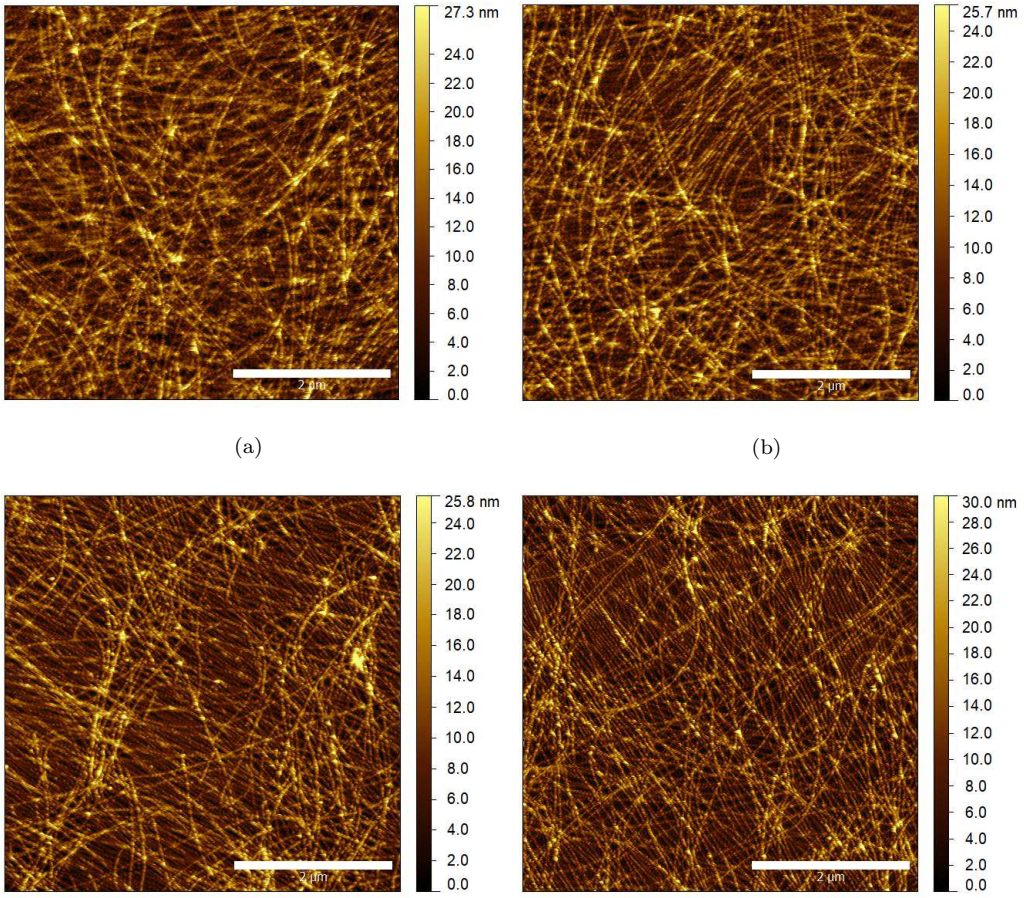

Figure 6: **AFM images of on-center spin coated samples.** Atomic force microscopy height images of one month aged $5mg/ml$ rr-P3HT in chlorobenzene, spin coated on-center at (a) $1000rpm$, (b) $2000rpm$, (c) $4000rpm$, and (d) $5000rpm$.

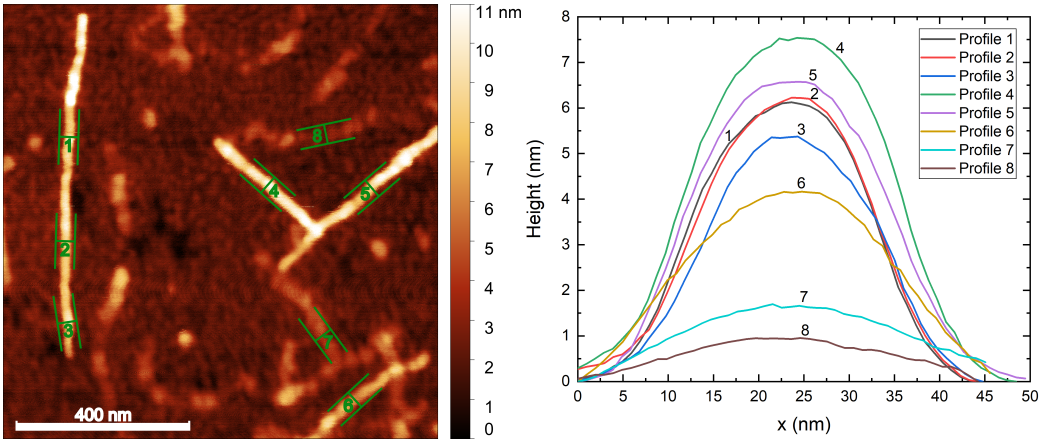

(a) (b)

Figure 7: **Analysis of nanowire dimensions via AFM.** (a) AFM image of a rr-P3HT film deposited from a 27 days aged solution, and (b) 8 height profiles of highlighted nanowires, averaged along a section of $130nm$ along the nanowire length with the software Gwyddion.

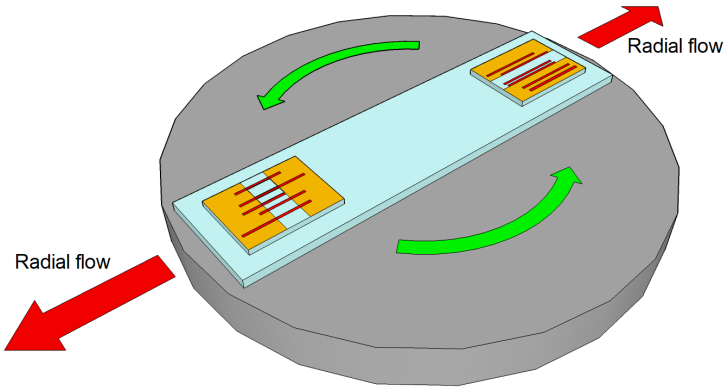

Figure 8: ***Graphical representation of the off-axis spin-coating technique.*** *Substrates are placed in one of the extremities of a glass slide to promote the alignment of nanowires (red). Note the different orientation of the gold electrodes substrates (yellow), so that the nanowires are aligned by centripetal forces either along (right) or across (left) the gap between electrodes.*

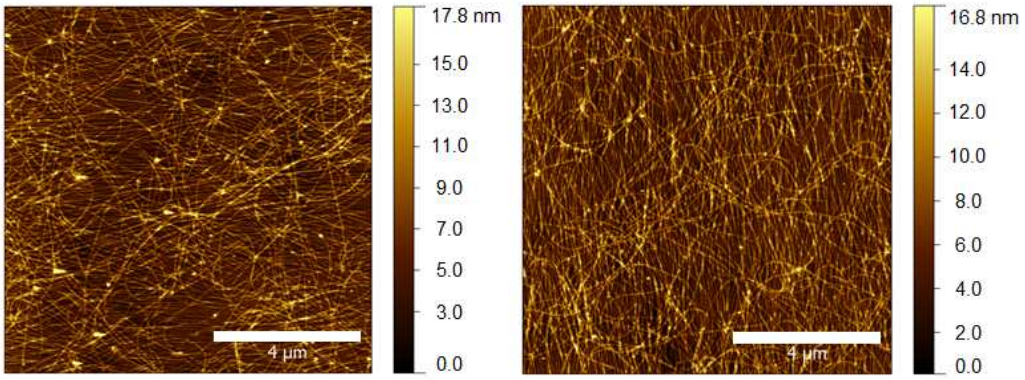

(a) (b)

Figure 9: ***AFM images of off-center spin coated samples.*** *Height images of the rr-P3HT films deposited from a one month aged solution onto electrode patterned glass substrates. Both images are oriented such that the electrodes are positioned to the left and right sides of the images resulting in films with nanowires aligned (a) across the gap (perpendicular to the electrodes), or (b) along the length of the gap (parallel to the electrodes).*

voltage data reported in figure 10 are split between the two configurations (averaging 5 samples each), and show resistances of $5.83M\Omega$ when nanowires are aligned parallel along the gap, and $3.83M\Omega$ when perpendicular across the gap. As expected, the current travels with greater ease along the length of the nanowires. This anisotropic conductivity exhibited by rr-P3HT suggests that the nanowires that are perpendicularly aligned across the gap between electrodes provide a more favorable path for the charge carriers to travel from one electrode to another, resulting in improved conductivity. On the other hand, in the samples where nanowires are aligned parallel to the channel, the charge carriers have to jump from nanowire to nanowire, or are restricted to the limited number of misaligned nanowires crossing the gap between electrodes. This preferential alignment is easily controlled during the production process, and can have beneficial effects for the properties of devices, because it significantly improves the electrical conductivity along the desired direction.

2.5. Grazing Incidence Wide Angle X-ray Scattering

The structural orientation of aligned rr-P3HT nanowires was also investigated by grazing-incidence wide angle x-ray scattering (GIWAXS). This was

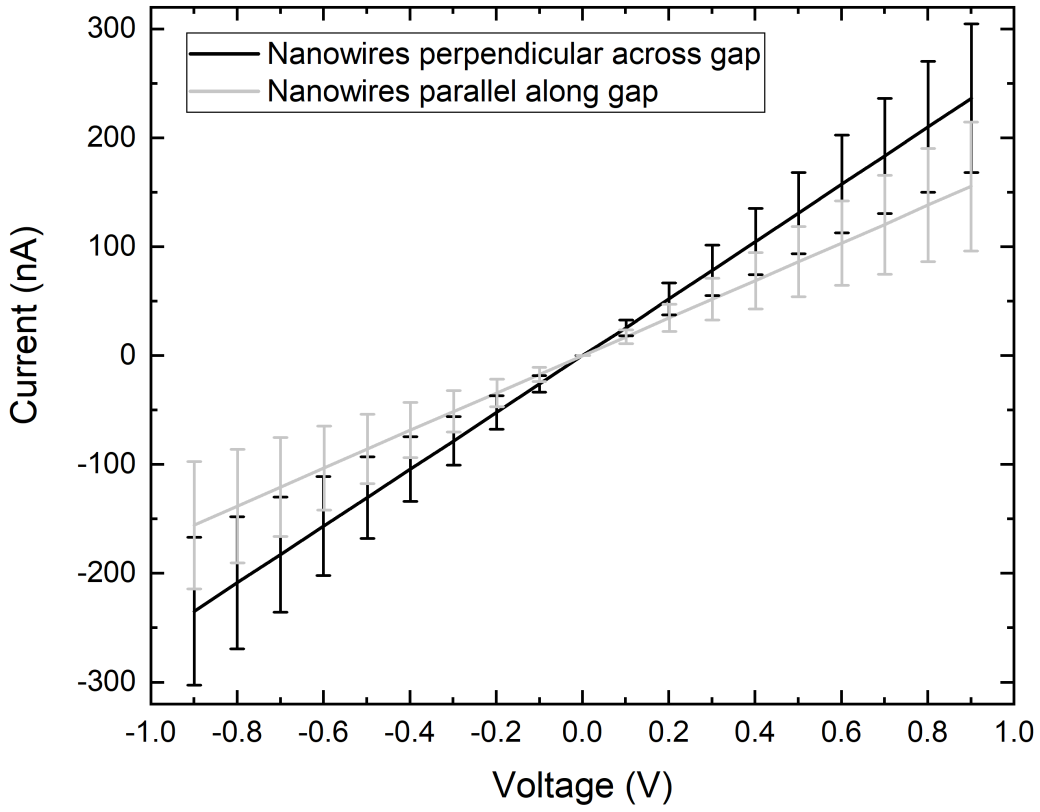

Figure 10: $I-V$ ***graph.*** *Averaged $I-V$ responses of the 10 samples of rr-P3HT nanowires. Each plot is an average of 5 samples, with those aligned parallel (gray) and those aligned perpendicular (black) to the gap.*

done using nanowire samples spin-coated onto Si substrates from a 1 month aged, $5mg/mL$ solution at $5000rpm$. Figure 11a shows the two-dimensional GIWAXS image of an on-center spin-coat sample, where nanowires are randomly aligned in the center of the substrate. The three distinctive peaks along the vertical out-of-plane direction at $Q_z \sim 0.39\mathring{A}^{-1}$, $Q_z \sim 0.78\mathring{A}^{-1}$, and $Q_z \sim 1.17\mathring{A}^{-1}$ correspond to the lamellar spacing in the (100), (200), and (300) axes, due to spacing between the polymer backbones as a results of the rr-P3HT side chains. The peak along the horizontal in-plane direction at $Q_x \sim 1.62\mathring{A}^{-1}$ corresponds to the π-π stacking in the (010) axis, as reported by others Sirringhaus (1999); Yang (2005). This preferential ordering of rr-P3HT chains is typical of an edge-on position in which the alkyl side-chains face the substrate Kwon (2014). We then analyzed two off-center spin-coat samples, one measured such that the x-ray beam was incident parallel to the direction of the nanowires and another one such that the x-ray beam was perpendicular to them. Figures 11b and 11c show the two-dimensional images of the x-ray scattering from the samples (having been corrected for the curved surface of the Ewald sphere), and figures 11d and 11e show one-dimensional radial integrations taken from the images either vertically in the out-of-plane direction Q_z, or horizontally along the in-plane direction Q_x. Both the GIWAXS images of the samples with aligned nanowires confirm the edge-on orientation of rr-P3HT polymer backbones evidenced by the three peaks at $Q_z \sim 0.39\mathring{A}^{-1}$, $Q_z \sim 0.78\mathring{A}^{-1}$, and $Q_z \sim 1.17\mathring{A}^{-1}$ in the out-of-plane direction due to the side chains spacing, and the $Q_x \sim 1.62\mathring{A}^{-1}$ peak in the in-plane direction, corresponding to π-π stacking in the (010) axis. All of the x-ray scattering features are more intense in the randomly oriented sample compared to the aligned samples which we attribute to a greater density of nanowires being present in the on-center sample due to reduced centripetal forces. According to the out of plane data, for the nanowires aligned across the x-ray beam direction, the peaks at $Q_z \sim 0.39\mathring{A}^{-1}$, $Q_z \sim 0.78\mathring{A}^{-1}$, and $Q_z \sim 1.17\mathring{A}^{-1}$ are more intense (approximately double) compared to the one in the sample where the nanowires run parallel to the beam direction. We attribute this increased scattering associated with lamellar stacking to the geometry of the measurement which samples a larger number of nanowires when they run across the beam. Furthermore, when comparing the in plane x-ray scattering, it is evident that the intensity of the peak at $0.39\mathring{A}^{-1}$ is stronger in the measurement across the nanowires, but the $1.62\mathring{A}^{-1}$ peak, if considered relative to the intensity of the $0.39\mathring{A}^{-1}$ peak, is stronger in the measurement where the x-ray beam is oriented along the length of the nanowires. We

attribute the relative increase in scattering on the $Q_x \sim 1.62\mathring{A}^{-1}$ peak to the parallel alignment of the nanowires with respect to the direction of the x-ray beam. Since the length of nanowires depends on π-π stacking (see figure 1b) the x-rays travelling along the nanowires are increasingly scattered by the repeating π-π stacks resulting in the relatively more intense peak shown by the in plane data.

3. Conclusions

In summary, we have been able to follow the formation of rr-P3HT nanostructures $in-situ$ in chlorobenzene solution via small angle neutron scattering, modelling the data using the Guinier-Porod equation, and we were able to directly link processing conditions (ageing, heating, cooling) to the nanostructure shape and morphology. Optical absorption spectroscopy revealed that crystallization is initially fast, but continues for a period of at least 13 days, albeit with a decreasing rate. We showed that the solution temperature significantly impacts nanowire formation and enables control over nanowire population. Low temperatures ($-2°C$ to $4°C$) for a suitable time period promote rr-P3HT elongation into rod structures, followed by stacking of these rods into lamellae and lamellae into nanowires, whilst high temperatures ($40-80°C$) disassemble these higher dimensionality structures. We also noticed that the dissolution rate is faster than the crystallization rate. Additionally, we deposited the nanowires as thin films via on-center and off-center spin coating, demonstrating the conditions to achieve alignment of nanowires, in particular in terms of spin coating speed and distance from the center of rotation. Such alignment and anisotropy were corroborated by AFM and grazing-incidence wide angle x-ray scattering. Finally, via $I-V$ characterization we demonstrated an improved conductivity of selectively aligned nanowires; therefore, the formation of crystalline phases such as lamellae and nanowires can have a significant impact. They have the potential to improve the performance in electronic devices, such as organic transistors and gas sensors. We demonstrated the existence of a close relationship between the thermal and temporal conditions of the rr-P3HT solution and the nanowire formation within it. This may well explain the large variations in performance when rr-P3HT is used to fabricate organic devices. To mitigate this it is important to accurately control the thermal history of the solution and the conditions of deposition, taking into account that for the production of devices the solutions are usually heated at $80°C$

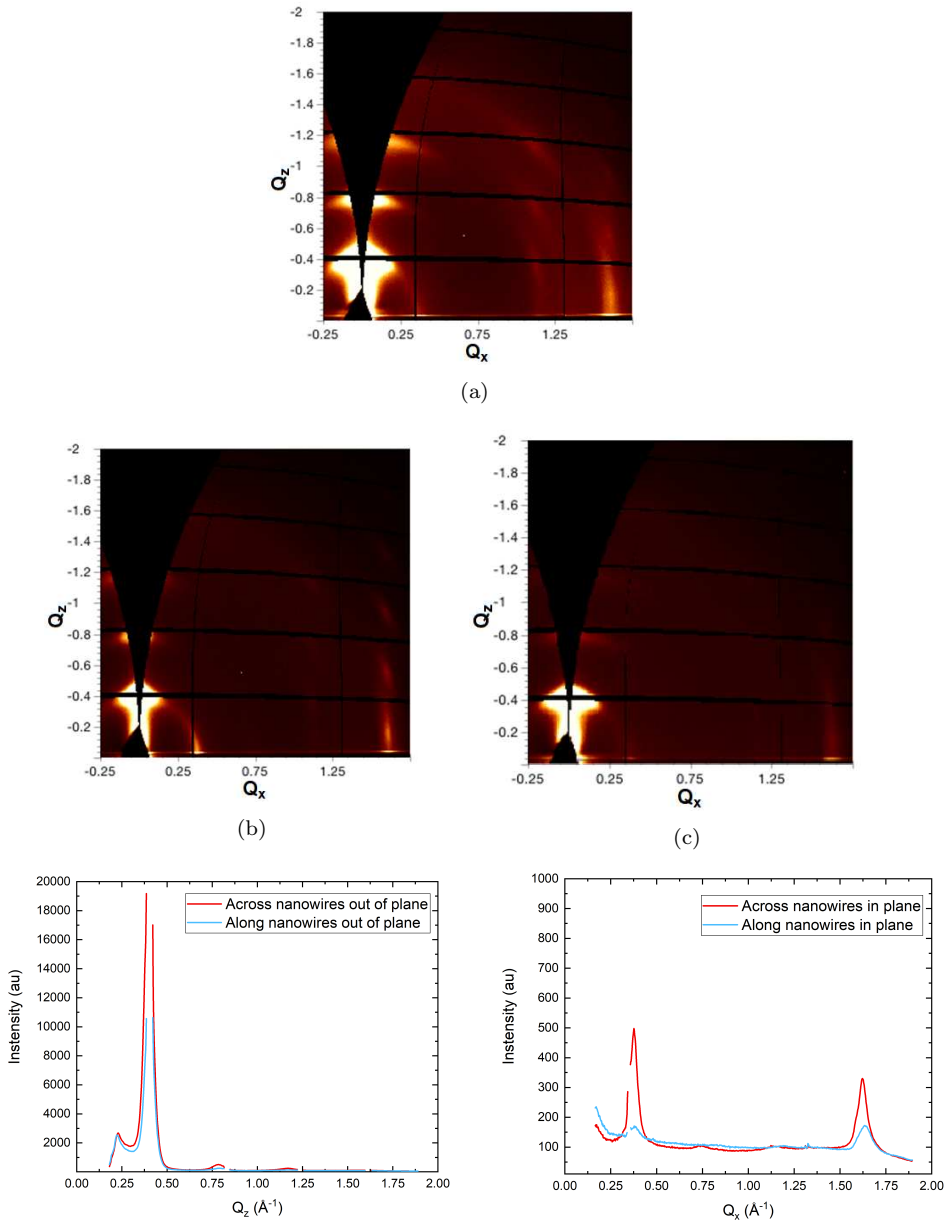

Figure 11: **GIWAXS data and profiles.** GIWAXS 2D graphs of rr-P3HT nanowires randomly aligned (a), predominantly aligned perpendicular to (across the nanowires) the x-ray beam (b), and predominantly aligned parallel (along the nanowires) to the x-ray beam (c). Vertical out-of-plane (d) and horizontal in-plane (e) 1D sector radial integration graphs are shown for the nanowires aligned perpendicular and parallel to the the x-ray beam.

in order to molecularly dissolve rr-P3HT.

4. Experimental

4.1. Preparation of P3HT solution

A number of rr-P3HT solutions with different concentrations were prepared by dissolving rr-P3HT (Ossila Ltd, M101, 96.6% regioregularity, $M_{\mathrm{w}} = 65,500$ and $M_{\mathrm{n}} = 32,000$) in chlorobenzene (Sigma Aldrich Ltd, 99% grade). The solutions were stirred for 10 minutes at $80°C$ and then left to cool for 5 minutes, before the solutions were filtered through a $0.45\mu m$ Whatman PTFE filter. They were stored before use in the dark at room temperature ($18°C$) and approximately 30% relative humidity for the required ageing period. For the AFM measurement in figure 7, a different batch of rr-P3HT was used (Ossila Ltd, M102, 95.6% regioregularity, $M_{\mathrm{w}} = 65,200$ and $M_{\mathrm{n}} = 29,600$). Slight variations in the rr-P3HT used for these measurements were noted with the solution requiring slightly lower temperature for nanowire formation. This was attributed to improved solubility due to the M_{w} and regioregularity differences. For the neutron scattering experiments, deuterated chlorobenzene (d_5, 99%) from Goss Scientific Instruments Ltd, was used as solvent to enhance the scattering contrast between the solvent and the rr-P3HT.

4.2. Nanowire Deposition and Alignment by Spin Coating

The nanowires produced in this study were spin coated either onto $15mm$ by $24mm$ Si wafer pieces for AFM and GIWAXS characterization, or onto glass substrates with lithographically defined gold electrode pads ($10\mu m$ spacing between the two electrical contact pads) for electrical characterization. All substrates were washed prior to use in an ultrasonic bath for 10 minutes in a 1% Hellmanex ™III/deionized water solution and subsequently in a 2-Propanol reflux unit. After the sonication, the substrates were rinsed twice in hot D.I. water and once in cold D.I. water. The substrates were then dried under a nitrogen gas flow and lastly cleaned with oxygen plasma for 5 minutes. $100\mu L$ of the rr-P3HT solution (containing nanowires) was then spin-coated at the required spin-speed for 1 minute, then the samples were left to dry in air at $18°C$ for 15 minutes.

4.3. Characterization methods

The optical absorption spectra of the solutions was obtained using a Mikropack UV-VIS-NIR mini D_2 light source ($350 - 850nm$) and an Ocean Optics USB 2000 spectrometer. The small angle neutron scattering (SANS) experiments were conducted using the SANS2D small-angle diffractometer Heenan (2011) at the ISIS Pulsed Neutron Source (STFC Rutherford Appleton Laboratory, Didcot, UK). A pulsed neutron beam with an incident wavelength range of $1.75 - 16.5\mathring{A}$ was directed through the samples simultaneously delivering a scattering q-range of $0.0045 - 0.75\mathring{A}^{-1}$ measured using a $1m^2$ detector offset vertically by $150mm$ and horizontally $180mm$. The samples were contained within quartz banjo cells (Hellma GmbH) with a $2mm$ path length. The temperature of the vials was controlled using a recirculating water bath. The diameter of the beam was $12mm$. The small angle scattering data collected were processed to correct for the detector response, transmission of the sample and background scatter, and reduced to a one dimensional plot of intensity versus momentum transfer using the Mantid data reduction software Arnold (2014). The intensity data were normalized to an absolute scale (cm^{-1}) which was determined by comparing with a standard sample (a solid blend of hydrogenous and perdeuterated polystyrene) in accordance with established procedures Wignall (1987). The atomic force microscopy (AFM) images were collected using a Veeco Dimension 3100 AFM with a Nanoscope IIIa controller and basic extender. The instrument was operated in tapping mode with Bruker TESPA tapping mode cantilevers, with a nominal spring constant of $42N/m$ and a nominal resonant frequency of $320kHz$. I-V curves were obtained with software developed in LabView and a Keithley 2400 voltage source meter. Grazing-incidence wide angle X-ray scattering (GIWAXS) experiments were conducted at the Diamond Light Source, beamline I07 (Didcot, UK). Here, a $8keV$ energy X-ray beam was incident on the sample surface at a grazing incidence angle of $0.22°$. The images were collected using a Pilatus 2M x-ray detector with a sample to detector distance of $337mm$. A purpose built sample chamber in which a steady low flow rate of helium gas was used to reduce background X-ray scattering housed the samples during the experiment. The resulting data were calibrated using a sample of silver behenate, and analyzed using DAWN x-ray analysis software.

Conflict of interest

Declarations of interest: none.

Acknowledgement

F.B. thanks the EPSRC Centre for Doctoral Training in New and Sustainable PV for the provision of a PhD scholarship (EP/L01551X/1). G.P thanks the National Council of Science and Technology (CONACyT) of Mexico and the Mexico Secretary of Energy (SENER) for the provision of a PhD scholarship. A.D. wishes to acknowledge support from the EPSRC through Supergen Solar Challenge Grant : EP/M025020/1. We also gratefully acknowledge the Science and Technology Facilities Council (STFC) for access to neutron beamtime at ISIS on SANS2D (RB:1310252), and also for the provision of sample preparation facilities. Finally we gratefully acknowledge the Diamond Light Source, beamline I07 (experiment SI8117-1) and Dr Jonathan Rawle for his help with the experiments.

Supporting Information Available

The following files are available free of charge:

- Filename: S.I. P3HTNW. Contains: All the parameters obtained from the Guinier-Porod model for the SANS analysis (table S1), SANS data and corresponding fits for the temperature and ageing analysis on P3HT nanowires formation (figures S1, S2, and S3)

References

M. Dang, L. Hirsch, G. Wantz, P3HT:PCBM, Best Seller in Polymer Photovoltaic Research, Adv. Mater. 23 (2011) 3597-3602. https://doi.org/10.1002/adma.201100792.

M. Onoda, K. Tada, Photoinduced Charge Transfer of Conducting Polymer Composites, IEICE T ELECTRON E81-C (1998) 1051-1056.

P. Berger, M. Kim, Polymer Solar Cells: P3HT:PCBM and Beyond, J. Renew. Sustain. Energy 10 (2018) 013508. https://doi.org/10.1063/1.5012992.

Y. Guo, C. Liu, K. Inoue, K. Harano, H. Tanaka, E. Nakamura, Enhancement in the Efficiency of an Organic-Inorganic Hybrid Solar Cell with a Doped P3HT Hole-Transporting Layer on a Void-Free Perovskite Active Layer, J. Mater. Chem. A 2 (2014) 13827-13830. https://doi.org/10.1039/C4TA02976C.

J. Xiao, J. Shi, H. Liu, Y. Xu, S. Lv, Y. Luo, D. Li, Q. Meng, Y. Li, Efficient $CH_3NH_3Pbl_3$ Perovskite Solar Cells Based on Graphdiyne (GD)-Modified P3HT Hole-transporting Material, Adv. Energy Mater 5 (2015) 1401943. https://doi.org/10.1002/aenm.201401943.

P. Zhou, T. Bu, S. Shi, L. Li, Y. Zhang, Z. Ku, Y. Peng, J. Zhong, Y.B. Cheng, F. Huang, Efficient and Stable Mixed Perovskite Solar Cells Using P3HT as a Hole Transporting Layer, J. Mater. Chem. C 6 (2018) 5733-5737. https://doi.org/10.1039/C8TC01345D.

C. Poelking, K. Daoulas, A. Troisi, D. Andrienko, Morphology and Charge Transport in P3HT: A theorist's Perspective, In: S. Ludwigs S. P3HT Revisited - From Molecular Scale to Solar Cell Devices, Adv. Polym Sci, Berlin, 2014, pp. 139-180.

F. Laquai, D. Andrienko, R. Mauer, P. Blom, Charge Carrier Transport and Photogeneration in P3HT:PCBM Photovoltaic Blends, Macromol. Rapid Commun. 36 (2015) 1001-1025. https://doi.org/10.1002/marc.201500047.

S. Agbolaghi, S. Zenoozi, A comprehensive Review on Poly(3-alkylthiophene)-Based Crystalline Structures, Protocols and Electronic Applications. Org. Electron. 51 (2017) 362-403. https://doi.org/10.1016/j.orgel.2017.09.038.

M. Wong-Stringer, J. Bishop, J. Smith, D. Mohamad, A. Parnell, V. Kumar, C. Rodenburg, D. Lidzey, Efficient Perovskite Photovoltaic Devices Using Chemically Doped PCDTBT as a Hole-Transport Material, J. Mater. Chem. A 5 (2017) 15714-15723. https://doi.org/10.1039/c7ta03103c.

Y. Zhang, E. Bovill, J. Kingsley, A. Buckley, H. Yi, A. Iraqi, T. Wang, D. Lidzey, PCDTBT Based Solar Cells: One Year of Operation Under Real-World Conditions, Sci. Rep. 6 (2016) 21632. https://doi.org/10.1038/srep21632.

S. Park, A. Roy, S. Beaupré, S. Cho, N. Coates, J. Moon, D. Moses, M. Leclerc, K. Lee, A. Heeger, Bulk Heterojunction Solar Cells with Internal Quantum Efficiency Approaching 100%, Nat. Photonics 3 (2009) 297-303. https://doi.org/10.1038/NPHOTON.2009.69.

C.K. Kwak, G.E. Perez, B.G. Freestone, S.A. Al-Isaee, A. Iraqi, D.G. Lidzey, A.D.F. Dunbar, Improved Efficiency in Organic Solar Cells Via Conjugated Polyelectrolyte Additive in the Hole Transporting Layer, J. Mater. Chem. C 4 (2016) 10722-10730. https://doi.org/10.1039/C6TC03771B.

L. Fernandes, H. Gaspar, J. Tomé, F. Figueira, G. Bernardo, Thermal Stability of Low-Bandgap Copolymers PTB7 and PTB7-Th and Their Bulk Heterojunction Composites, Polym. Bull 75 (2018) 515-532. https://doi.org/10.1007/s00289-017-2045-8.

Y. Liang, Z. Xu, J. Xia, S.T. Tsai, Y. Wu, G. Li, C. Ray, L. Yu, For the Bright Future-Bulk Heterojunction Polymer Solar Cells with Power Conversion Efficiency of 7.4%, Adv. Mater. 22 (2010) E135-E138. https://doi.org/10.1002/adma.200903528.

L. Lu, L. Yu, Understanding Low Bandgap Polymer PTB7 and Optimizing Polymer Solar Cells Based on It, Adv. Mater. 26 (2014) 4413-4430. https://doi.org/10.1002/adma.201400384.

K. Wang, C. Liu, P. Du, H.L. Zhang, X. Gong, Efficient Perovskite Hybrid Solar Cells Through a Homogeneous High-Quality Organolead Iodide Layer, Small 11 (2015) 3369-3376. https://doi.org/10.1002/smll.201403399.

X. Hu, P. Du, W. Xu, K. Wang, C. Yi, C. Liu, F. Huang, X. Gong, Y. Cao, Efficient Perovskite Hybrid Solar Cells via Controllable Crystallization Film Morphology, IEEE J. Photovolt. 5 (2015) 1402-1407. https://doi.org/10.1109/JPHOTOV.2015.2455345.

M. Wong-Stringer, O.S. Game, J.A. Smith, T.J. Routledge, B.A. Alqurashy, B.G. Freestone, A.J. Parnell, N. Vaenas, V. Kumar, M.O.A. Alawad, A. Iraqi, C. Rodenburg, D.G. Lidzey, High-Performance Multilayer Encapsulation for Perovskite Photovoltaics, Adv. Energy Mater 8 (2018) 1801234. https://doi.org/10.1002/aenm.201801234.

P.H. Chu, N. Kleinhenz, N. Persson, M. McBride, J.L. Hernandez, B. Fu, G. Zhang, E. Reichmanis, Toward Precision Control of Nanofiber Orientation in Conjugated Polymer Thin Films: Impact on Charge Transport, Chem. Mater. 28 (2016) 9099-9109. https://doi.org/10.1021/acs.chemmater.6b04202.

J. Jeong, Y. Park, J. Choi, T. Park, H. Choi, E. Song, B. Ju, J. Lee, H. Chu, p-174: The Electrical Properties of Transparent Emotional OLED Lighting Based on Organic Environment Sensor, 49th Annual SID Symposium, Seminar, and Exhibition 2011, Display Week 2011 3 (2011) 1753-1756. https://doi.org/10.1889/1.3621230.

A. Roigé, M. Campoy-Quiles, J. Ossó, M. Alonso, L. Vega, M. Garriga, Surface vs Bulk Phase Transitions in Semiconducting Polymer Films for OPV and OLED Applications, Synth. Met. 161 (2012) 2570-2574. https://doi.org/10.1016/j.synthmet.2011.09.031.

S. Kumar, C. Borriello, G. Nenna, R. Rosentsveig, T. Di Luccio, Dispersion of WS_2 Nanotubes and Nanoparticles Into Conducting Polymer Matrices for Application as LED Materials, Eur. Phys. J. B 85 (2012) 160. https://doi.org/10.1140/epjb/e2012-20453-4.

D.L. Ellis, M.R. Zakin, L.S. Bernstein, M.F. Rubner, Conductive Polymer Films as Ultrasensitive Chemical Sensors for Hydrazine and Monomethylhydrazine Vapor, Anal. Chem. 68 (1996) 817-822. https://doi.org/10.1021/ac950662k.

S.H. Chan, T.F. Lin, M.C. Wu, S.H. Chen, W.F. Su, C.S. Lai, Using Aligned Poly(3-Hexylthiophene)/Poly(Methyl Methacrylate) Blend Fibers to Detect Volatile Organic Compounds, Jpn. J. Appl. Phys 57 (2018) 04FM06. https://doi.org/10.7567/JJAP.57.04FM06.

J. Im, S. Sengupta, M. Baruch, C. Granz, S. Ammu, S. Manohar, J. Whitten, A Hybrid Chemiresistive Sensor System for the Detection of Organic Vapors, Sensors and Actuators, B: Chemical 156 (2011) 715-722. https://doi.org/10.1016/j.snb.2011.02.025.

N. Seidler, G. Lazzerini, G. Li Destri, G. Marletta, F. Cacialli, Enhanced Crystallinity and Film Retention of P3HT Thin-Films for Efficient Organic

Solar Cells by Use of Preformed Nanofibers in Solution, J. Mater. Chem. C 1 (2013) 7748-7757. https://doi.org/10.1039/C3TC31284D.

Z. Bao, A. Dodabalapur, A. Lovinger, Soluble and Processable Regioregular Poly(3-Hexylthiophene) for Thin Film Field-Effect Transistor Applications With High Mobility, Appl. Phys. Lett. 69 (1996) 4108-4110. https://doi.org/10.1063/1.117834.

M. Surin, P. Leclére, R. Lazzaroni, J. Yuen, G. Wang, D. Moses, A. Heeger, S. Cho, K. Lee, Relationship Between the Microscopic Morphology and the Charge Transport Properties in Poly(S-Hexylthiophene) Field-Effect Transistors, J. Appl. Phys. 100 (2006). https://doi.org/10.1063/1.2222065.

S. Joshi, S. Grigorian, U. Pietsch, P. Pingel, A. Zen, D. Neher, U. Scherf, Thickness Dependence of the Crystalline Structure and Hole Mobility in Thin Films of Low Molecular Weight Poly(3-hexylthiophene), Macromolecules 41 (2008) 6800-6808. https://doi.org/10.1021/ma702802x.

C.H. Woo, C. Piliego, T.W. Holcombe, M.F. Toney, J.M.J. Fréchet, A Quantitative Correlation between the Mobility and Crystallinity of Photo-Cross-Linkable P3HT, Macromolecules 45 (2012) 3057-3062. https://doi.org/10.1021/ma202203z.

C. Poelking, D. Andrienko, Effect of Polymorphism, Regioregularity and Paracrystallinity on Charge Transport in Poly(3-hexylthiophene) [P3HT] Nanofibers, Macromolecules 46 (2013) 8941-8956. https://doi.org/10.1021/ma4015966.

G.M. Newbloom, P. de la Iglesia, L.D. Pozzo, Controlled gelation of poly(3-alkylthiophene)s in bulk and in thin-films using low volatility solvent/poor-solvent mixtures, Soft Matter 10 (2014) 8945. https://doi.org/10.1039/c4sm00960f.

J.A. Merlo, C.D. Frisbie, Field Effect Transport and Trapping in Regioregular Polythiophene Nanofibers, The J. Phys. Chem. B 108 (2004) 19169-19179. https://doi.org/10.1021/jp047023a.

S. Dag, L.W. Wang, Packing Structure of Poly(3-hexylthiophene) Crystal: Ab Initio and Molecular Dynamics Studies, The J. Phys. Chem. B 114 (2010) 5997-6000. https://doi.org/10.1021/jp1008219.

N. Kleinhenz, C. Rosu, S. Chatterjee, M. Chang, K. Nayani, Z. Xue, E. Kim, J. Middlebrooks, P.S. Russo, J.O. Park, M. Srinivasarao, E. Reichmanis, Liquid Crystalline Poly(3-hexylthiophene) Solutions Revisited: Role of Time-Dependent Self-Assembly, Chem. Mater. 27 (2015) 2687-2694. https://doi.org/10.1021/acs.chemmater.5b00635.

J.Y. Oh, M. Shin, T.I. Lee, W.S. Jang, Y. Min, J.M. Myoung, H.K. Baik, U. Jeong, Self-Seeded Growth of Poly(3-hexylthiophene) (P3HT) Nanofibrils by a Cycle of Cooling and Heating in Solutions, Macromolecules 45 (2012) 7504-7513. https://doi.org/10.1021/ma300958n.

S. Han, X. Yu, W. Shi, X. Zhuang, J. Yu, Solvent-Dependent Electrical Properties Improvement of Organic Field-Effect Transistor Based on Disordered Conjugated Polymer/Insulator Blends, Org. Electron. 27 (2015) 160-186. https://doi.org/10.1016/j.orgel.2015.09.003.

J.F. Chang, B. Sun, D.W. Breiby, M.M. Nielsen, T.I. Sölling, M. Giles, I. McCulloch, H. Sirringhaus, Enhanced Mobility of Poly(3-hexylthiophene) Transistors by Spin-Coating from High-Boiling-Point Solvent, Chem. Mater. 16 (2004) 4772-4776. https://doi.org/10.1021/cm049617w.

J.H. Kim, J.H. Park, J.H. Lee, J.S. Kim, M. Sim, C. Shim, K. Cho, Bulk Heterojunction Solar Cells Based on Preformed Polythiophene Nanowires Via Solubility-Induced Crystallization, J. Mater. Chem. 20 (2010) 7398-7405. https://doi.org/10.1039/C0JM00666A.

Y. Xi, D.S. Li, G.M. Newbloom, W.K. Tatum, M. O'Donnel, C.K. Luscombe, L.D. Pozzo, Sonocrystallization of conjugated polymers with ultrasound fields, Soft Matter 14 (2018) 4963. https://doi.org/10.1039/C8SM00905H.

Y. Diao, L. Shaw, Z. Bao, S.C.B. Mannsfeld, Morphology Control Strategies for Solution-Processed Organic Semiconductor Thin Films, Energy Environ. Sci. 7 (2014) 2145-2159. https://doi.org/10.1039/C4EE00688G.

H.E. Katz, Recent Advances in Semiconductor Performance and Printing Processes for Organic Transistor-Based Electronics, Chem. Mater 16 (2004) 4748-4756. https://doi.org/10.1021/cm049781j.

S. Cho, K. Lee, J. Yuen, G. Wang, D. Moses, A.J. Heeger, M. Surin, R. Lazzaroni, Thermal Annealing-Induced Enhancement of the Field-Effect

Mobility of Regioregular Poly (3-hexylthiophene) Films, J. Appl. Phys. 100 (2006) 114503. https://doi.org/10.1063/1.2400796.

Y. Cui, Z. Zhong, D. Wang, W.U. Wang, C.M. Lieber, High Performance Silicon Nanowire Field Effect Transistors, Nano Lett. 3 (2003) 149-152. https://doi.org/10.1021/nl025875l.

C.M. Fu, K.S. Jeng, Y.H. Li, Y.C. Hsu, M.H. Chi, W.B. Jian, J.T. Chen, Effects of Thermal Annealing and Solvent Annealing on the Morphologies and Properties of Poly (3-hexylthiophene) Nanowires, Macromol. Chem. Phys. 216 (2015) 59-68. https://doi.org/10.1002/macp.201400315.

K.C. Dickey, J.E. Anthony, Y.L. Loo, Improving Organic Thin-Film Transistor Performance Through Solvent-Vapor Annealing of Solution-Processable Triethylsilylethynyl Anthradithiophene, Adv. Mater. 18 (2006) 1721-1726. https://doi.org/10.1002/adma.200600188.

Z. Hu, T. Adachi, R. Haws, B. Shuang, R.J. Ono, C.W. Bielawski, C.F. Landes, P.J. Rossky, D.A. Vanden Bout, Excitonic Energy Migration in Conjugated Polymers: The critical Role of Interchain Morphology, J. Am. Chem. Soc. 136 (2014) 16023-16031. https://doi.org/10.1021/ja508112k.

M.G. Newbloom, F.S. Kim, S.A. Jenekhe, D.C. Pozzo, Mesoscale Morphology and Charge Transport in Colloidal Networks of Poly(3-hexylthiophene), Macromolecules 44 (2011) 3801-3809. https://doi.org/10.1021/ma2000515.

G.M. Newbloom, K.M. Weigandt, D.C. Pozzo, Structure and property development of poly(3-hexylthiophene) organogels probed with combined rheology, conductivity and small angle neutron scattering, Soft Matter 8 (2012) 8854. https://doi.org/10.1039/C2SM26114F.

J.K. Keum, K. Xiao, I.N. Ivanov, K. Hong, J.F. Browning, G.S. Smith, M. Shao, K.C. Littrell, A.J. Rondinone, E.A. Payzant, J. Chenb, D.K. Hensley, Solvent quality-induced nucleation and growth of parallelepiped nanorods in dilute poly(3-hexylthiophene) (P3HT) solution and the impact on the crystalline morphology of solution-cast thin film, CrystEngComm 15 (2013) 1114. https://doi.org/10.1039/C2CE26666K.

G. Bernardo, A.L. Washington, Y. Zhang, S.M. King, D.T.W. Toolan, M.P. Weir, A.D.F. Dunbar, J.R. Howse, R. Dattani, J.P.A. Fair-

clough, A.J. Parnell, Does 1,8-Diodooctane (DIO) Affect the Aggregation State of PC71BM in Solution?, R. Soc. open sci 5 (2018) 180937. https://doi.org/10.1098/rsos.180937.

B. Dörling, V. Vohra, T.T. Dao, M. Garriga, H. Murata, M. Campoy-Quiles, Uniaxial Macroscopic Alignment of Conjugated Polymer Systems by Directional Crystallization During Blade Coating, J. Mater. Chem. C 2 (2014) 3303-3310. https://doi.org/10.1039/C3TC32056A.

M.J. Lee, D. Gupta, N. Zhao, M. Heeney, I. McCulloch, H. Sirringhaus, Anisotropy of Charge Transport in a Uniaxially Aligned and Chain-Extended, High-Mobility, Conjugated Polymer Semiconductor, Adv. Funct. Mater. 21 (2011) 932-940. https://doi.org/10.1002/adfm.201001781.

G. Giri, D.M. DeLongchamp, J. Reinspach, D.A. Fischer, L.J. Richter, J. Xu, S. Benight, A. Ayzner, M. He, L. Fang, G. Xue, M.F. Toney, Z. Bao, Effect of Solution Shearing Method on Packing and Disorder of Organic Semiconductor Polymers, Chem. Mater. 27 (2015) 2350-2359. https://doi.org/10.1021/cm503780u.

J.Y. Na, B. Kang, D.H. Sin, K. Cho, Y.D. Park, Understanding Solidification of Polythiophene Thin Films During Spin-Coating: Effects of Spin-Coating Time and Processing Additives, Sci. Rep. 5 (2015) 13288. https://doi.org/10.1038/srep13288.

L.H. Jimison, M.F. Toney, I. McCulloch, M. Heeney, A. Salleo, Charge-Transport Anisotropy Due to Grain Boundaries in Directionally Crystallized Thin Films of Regioregular Poly (3-hexylthiophene), Adv. Mater. 21 (2009) 1568-1572. https://doi.org/10.1002/adma.200802722.

M. Chang, D. Choi, B. Fu, E. Reichmanis, Solvent Based Hydrogen Bonding: Impact on Poly (3-hexylthiophene) Nanoscale Morphology and Charge Transport Characteristics, ACS nano 7 (2013) 5402-5413. https://doi.org/10.1021/nn401323f.

Y. Xi, L.D. Pozzo, Electric field directed formation of aligned conjugated polymer fibers, Soft Matter 13 (2017) 3894. https://doi.org/10.1039/C7SM00485K.

Y. Yuan, G. Giri, A. Ayzner, A. Zoombelt, S. Mannsfeld, J. Chen, D. Nordlund, M. Toney, J. Huang, Z. Bao, Ultra-High Mobility Transparent Organic Thin Film Transistors Grown by an Off-Centre Spin-Coating Method, Nat. Commun. 5 (2014) 3005. https://doi.org/10.1038/ncomms4005.

N.K. Kim, S.Y. Jang, G. Pace, M. Caironi, W.T. Park, D. Khim, J. Kim, D.Y. Kim, Y.Y. Noh, High-Performance Organic Field-Effect Transistors with Directionally Aligned Conjugated Polymer Film Deposited from Pre-Aggregated Solution, Chem. Mater. 27 (2015) 8345-8353. https://doi.org/10.1021/acs.chemmater.5b03775.

Z. Fei, P. Boufflet, S. Wood, J. Wade, J. Moriarty, E. Gann, E.L. Ratcliff, C.R. McNeill, H. Sirringhaus, J.S. Kim, M. Heeney, Influence of Backbone Fluorination in Regioregular Poly (3-alkyl-4-fluoro) thiophenes, J. Am. Chem. Soc. 137 (2015) 6866-6879. https://doi.org/10.1021/jacs.5b02785.

V. Shrotriya, J. Ouyang, R.J. Tseng, G. Li, Y. Yang, Absorption Spectra Modification in Poly (3-hexylthiophene): Methanofullerene Blend Thin Films, Chem. Phys. Lett. 411 (2005) 138-143. https://doi.org/10.1016/j.cplett.2005.06.027.

K. Zhao, L. Xue, J. Liu, X. Gao, S. Wu, Y. Han, Y. Geng, A New Method to Improve Poly(3-hexyl thiophene) (P3HT) Crystalline Behavior: Decreasing Chains Entanglement To Promote Order-Disorder Transformation in Solution, Langmuir 26 (2010) 471-477. https://doi.org/10.1021/la903381f.

B.G. Kim, U. Kwon, D.H. Park, H.J. Park, Nano-Geometry Dependent Electrical Property of Organic Semiconductor, Electron. Mater. Lett. 11 (2015) 435-439. https://doi.org/10.1007/s13391-014-4457-z.

B. Hammouda, A new Guinier-Porod Model, J. Appl. Crystallogr. 43 (2010) 716-719. https://doi.org/10.1107/S0021889810015773.

B. Hammouda, Analysis of the Beaucage Model, J. Appl. Crystallogr. 43 (2010) 1474-1478. https://doi.org/10.1107/S0021889810033856.

A. Guiner, G. Fournet, C. Walker, Small angle scattering of X-rays, J. Wiley & Sons, New York, 1955.

L.A. Feigin, D.I. Svergun, Structure Analysis by Small-Angle X-Ray and Neutron Scattering, Springer, 1987.

O. Glatter, O. Kratky, Small-Angle X-Ray Scattering, Academic Press, London, 1982.

S. Malik, A.K. Nandi, Thermodynamic and Structural Investigation of Thermoreversible Poly(3-dodecyl thiophene) Gels in the Three Isomers of Xylene, J. Phys. Chem. B 108 (2004) 597-604. https://doi.org/10.1021/jp036590f.

K. Heo, C. Miesch, J.H. Na, T. Emrick, R.C. Hayward, Assembly of P3HT/CdSe nanowire networks in an insulating polymer host, Soft Matter 14 (2018) 5327. https://doi.org/10.1039/c8sm01001c.

W.D. Oosterbaan, V. Vrindts, S. Berson, S. Guillerez, O. Douhéret, B. Ruttens, J. D'Haen, P. Adriaensens, J. Manca, L. Lutsen, D. Vanderzande, Efficient Formation, Isolation and Characterization of Poly(3-alkylthiophene) Nanofibres: Probing Order as a Function of Side-Chain Length, J. Mater. Chem. 19 (2009) 5424-5435. https://doi.org/10.1039/B900670B.

H. Sirringhaus, P. Brown, R. Friend, M.M. Nielsen, K. Bechgaard, B. Langeveld-Voss, A. Spiering, R.A. Janssen, E. Meijer, P. Herwig, D. Leeuw, Two-Dimensional Charge Transport in Self-Organized, High-Mobility Conjugated Polymers, Nature 401 (1999) 685. https://doi.org/10.1038/44359.

H. Yang, T.J. Shin, L. Yang, K. Cho, C.Y. Ryu, Z. Bao, Effect of Mesoscale Crystalline Structure on the Field-Effect Mobility of Regioregular Poly (3-hexyl thiophene) in Thin-Film Transistors, Adv. Funct. Mater. 15 (2005) 671-676. https://doi.org/10.1002/adfm.200400297.

S. Kwon, K. Yu, K. Kweon, G. Kim, J. Kim, H. Kim, Y.R. Jo, B.J. Kim, J. Kim, S.H. Lee, L. Kwanghee, Template-Mediated Nano-Crystallite Networks in Semiconducting Polymers, Nat. Commun. 5 (2014) 4183. https://doi.org/10.1038/ncomms5183.

R.K. Heenan, S.E. Rogers, D. Turner, A.E. Terry, J. Treadgold, S.M. King, Small Angle Neutron Scattering Using Sans2d, Neutron News 22 (2011) 19-21. https://doi.org/10.1080/10448632.2011.569531.

O. Arnold, J.C. Bilheux, J.M. Borreguero, A. Buts, S.I. Campbell, L. Chapon, M. Doucet, N. Draper, R. Ferraz Leal, M.A. Gigg, V.E. Lynch, A. Markvardsen, D.J. Mikkelson, R.L. Mikkelson, R. Miller, K. Palmen, P. Parker, G. Passos, T.G. Perring, P.F. Peterson, S.Ren, M.A. Reuter, A.T. Savici, J.W. Taylor, R.J. Taylor, R. Tolchenov, W. Zhou, J. Zikovsky, Mantid-Data Analysis and Visualization Package for Neutron Scattering and μ SR Experiments, Nucl. Instrum. Methods Phys. Res. A 764 (2014) 156-166. https://doi.org/10.1016/j.nima.2014.07.029.

G. Wignall, F. Bates, Absolute Calibration of Small-Angle Neutron Scattering Data, J. Appl. Crystallogr. 20 (1987) 28-40. https://doi.org/10.1107/S0021889887087181.